Geophys. J. Int. (2003) **154,** 166–178

A synthesis of seismic *P* and *S* anisotropy

Vera Schulte-Pelkum[1] and Donna K. Blackman[2]

[1] *CIRES and Department of Geological Sciences, University of Colorado at Boulder, Boulder,* CO 80309, *USA. E-mail: vera_sp@cires.colorado.edu*
[2] *Institute of Geophysics and Planetary Physics, Scripps Institution of Oceanography, University of California, San Diego, La Jolla,* CA 92093, *USA*

Accepted 2003 February 15. Received 2003 February 5; in original form 2002 May 29

SUMMARY

Upper-mantle seismic anisotropy has been observed using a variety of methods, including *S* and *SKS* splitting, *P* and P_n traveltimes, *P* polarization anomalies and *P* to *S* conversions, and surface waves. Care must be taken when comparing the results from different methods because of bias introduced by depth sensitivity, frequency dependence, and simplifying assumptions concerning the form of anisotropy. We examine the differences and show that some apparent contradictions cited in previous studies can be reconciled using simple models. We perform forward modelling on a suite of anisotropic media, progressing from simple elastic symmetries to tensors obtained from laboratory measurements and numerical strain models. The results provide a systematic overview of the effect of a given anisotropy class and geometry on seismic observables. We simulate the full complement of body wave measurements—*SKS* and *S* splitting, P_n traveltimes, teleseismic *P* traveltimes and teleseismic *P* particle motion ($P_{\rm pol}$)—to show any apparent differences between the phases. We also investigate depth and frequency sensitivity using reflectivity modelling in layered anisotropic media. Our principal findings are as follows. (1) No models, including low-order symmetries and multiple layers, exhibit a mean fast shear wave splitting direction nearly orthogonal to a consistent fast direction determined from *P* observables. For *P* delays, the azimuthal $\cos(2\theta)$ variation is representative of the fast direction of anisotropy (rather than $\cos(1\theta)$, which has led to a certain amount of confusion in the literature). (2) *P* times average linearly over the raypath; *SKS* weights toward the upper part of the model; and $P_{\rm pol}$ and P_n are even more sensitive to shallow anisotropy. Conclusive evidence in the literature for a disagreement between fast directions from *SKS*, on one hand, and P_n and $P_{\rm pol}$, on the other hand, can be explained by layering. (3) The azimuthal dependence of *SKS* splitting results does not necessarily indicate layered or laterally heterogeneous anisotropy. The azimuthal dependence of *SKS* splitting is not observed for hexagonal symmetry with horizontal fast or slow axes, but has to be taken into consideration for dipping hexagonal and any orthorhombic and lower symmetry media. Teleseismic *S* shows a much stronger azimuthal dependence than *SKS* and *SKKS*. This makes procedures that stack splitting results over a wide range of incidence angles or azimuths questionable.

Key words: anisotropy, body waves, polarization, shear wave splitting, upper mantle.

1 INTRODUCTION

Measurements of upper-mantle anisotropy from *SKS* splitting have been published for nearly every region where seismic three-component stations exist (see, e.g., the compilations in Silver 1996; Savage 1999). To a lesser extent, mantle anisotropy has also been studied using P_n (Bamford 1977 and more recently, Smith & Ekström 1999; Hearn 1996, 1999) and teleseismic *P* traveltimes (e.g. Dziewonski & Anderson 1983; Babuska *et al.* 1984; Wylegalla *et al.* 1988; Gresillaud & Cara 1996).

Because of its conversion from *P* to *S* at the core–mantle boundary (CMB), *SKS* is known to be radially polarized initially (provided the CMB has no lateral structure) and its splitting is limited to the receiver side of the raypath, which makes it more attractive for anisotropy studies than teleseismic *S*. However, because the splitting is a cumulative effect, *SKS* offers technically no depth resolution between the CMB and receiver. A Fresnel zone argument can be made that most of the splitting occurs in the uppermost mantle, although anisotropy in the transition zone and in D″ may also have to be considered (Kendall 2000). In contrast to the lack of depth resolution, the steepness of *SKS* paths results in good lateral resolution, of the order of 50 km (Savage 1999).

Surface waves can be used in conjunction with *SKS* to constrain anisotropy (Montagner *et al.* 2000). In practice, however, global

surface wave maps have a rather large resolution limit of ∼2000 km laterally, while regional studies with a resolution scale of about 400 km are just beginning to appear in the literature.

There are other, less frequently used body wave diagnostics for anisotropy that can be used in conjunction with *SKS* to improve depth resolution. While the sensitivity range of teleseismic *P* traveltimes is comparable to that of *SKS*, P_n is confined to the uppermost mantle and *P* particle motion ($P_{\rm pol}$) samples anisotropy within one wavelength of the receiver (Schulte-Pelkum *et al.* 2001). Conversions between *P* and *S* at mantle discontinuities have also been used to investigate anisotropy (e.g. Levin & Park 1997; Frederiksen & Bostock 2000) but will be omitted from this discussion.

In addition to aiding depth resolution, phases other than *SKS* can also help detect cases where the assumption of the simplest anisotropy symmetry system with horizontal orientation frequently used in *SKS* analysis does not hold. Several studies have observed near 90° disagreement between fast directions determined from *SKS* splitting and *P* observations (see, e.g., Makeyeva *et al.* 1990, Guilbert *et al.* 1996 for *P* times, Smith & Ekström (1999) for P_n, Schulte-Pelkum *et al.* 2001 for $P_{\rm pol}$). Current seismological data sets allow a much more comprehensive study of anisotropy than individual methods, or even more limited *SKS* studies using a small number of events or backazimuths, can provide. To establish a basis for comparison between different methods, we conducted a systematic survey of the effects of progressively more complex anisotropy models on various body wave observables using two forward modelling approaches.

2 MODELLING: HOMOGENEOUS MEDIUM

In any given homogeneous anisotropic medium, all observables are based on two quantities, namely phase velocities and polarizations, given a direction of incidence. Following Shearer (1999), we consider a plane wave, $\mathbf{u} = \mathbf{a}\ \mathrm{e}^{-i\omega(t-\mathbf{s}\cdot\mathbf{x})}$, where $\mathbf{a}$ is the polarization (particle motion) vector and the slowness vector $\mathbf{s}$ has direction $\hat{\mathbf{s}}$ and length $1/c$, with c being the phase velocity. Substituting this solution into the momentum equation, $\rho\ddot{u}_i = \partial_j\sigma_{ij}$ (ρ = density, σ = stress), with the stress–strain relation $\sigma_{ij} = C_{ijkl}\varepsilon_{kl}$, where C_{ijkl} is the elastic tensor and ε is strain, and using $\varepsilon_{kl} = \frac{1}{2}(\partial_k u_l + \partial_l u_k)$ and the symmetry relations for the elasticity tensor, $C_{ijkl} = C_{jikl} = C_{ijlk} = C_{klij}$, we arrive at

$$\rho a_i = a_k C_{ijkl} s_j s_l. \tag{1}$$

If we define the density normalized elastic tensor projected on to the incident slowness direction as $M_{ij} = \frac{1}{\rho}C_{ijkl}\hat{s}_j\hat{s}_l$, then our problem of solving for the phase velocity c and polarization vector $\mathbf{a}$ is posed as the eigenproblem for the symmetric 3×3 matrix $\mathbf{M}$:

$$\mathbf{M}\mathbf{a} = c^2\mathbf{a}. \tag{2}$$

This eigenproblem has three solutions that correspond to a quasi-*P* (*qP*) and two quasi-*S* (*qS*) waves and it is simple to solve numerically. $\mathbf{M}$ is, by some, referred to as the Christoffel tensor or matrix and eq. (2) as the Christoffel equation (Babuska & Cara 1991).

We calculate the *qP* and *qS* solutions for a set of slowness directions sweeping out the entire azimuthal range as well as the range of incidence angles relevant for each phase under consideration. In the uppermost mantle, the incidence angle is horizontal for P_n, 20°–40° from the vertical for teleseismic *P*, 3°–13° for *SKS* and up to 17° for *SKKS*. For comparison, we also give the results for teleseismic *S* within the shear wave window (20°–40° at the Moho; Savage 1999). Teleseismic *S* is sometimes used to supplement coverage with *SKS* when the results are assumed to be consistent (Plomerova *et al.* 1998; Savage & Silver 1993).

Table 1. Elastic coefficients C_{ij} (GPa) used in Section 2.

i	*j*	Hex. fast	Hex. slow	Orthorhombic	Triclinic	Petrological
1	1	241.3	241.3	222.9	260.9	237.1
2	2	197.6	197.6	196.4	228.7	208.8
3	3	197.6	241.3	185.1	207.8	192.1
4	4	60.5	60.5	60.7	72.2	63.3
5	5	73.9	73.9	64.9	75.6	68.5
6	6	73.9	60.5	65.1	83.5	72.6
1	2	71.7	98.5	63.5	68.4	73.5
1	3	71.7	93.6	62.8	65.2	69.9
1	4	0.0	0.0	0.0	2.0	−0.2
1	5	0.0	0.0	0.0	−0.4	−0.6
1	6	0.0	0.0	0.0	−1.3	−0.3
2	3	76.6	98.5	65.1	72.0	72.3
2	4	0.0	0.0	0.0	0.9	−0.2
2	5	0.0	0.0	0.0	1.1	0.3
2	6	0.0	0.0	0.0	−0.7	−0.3
3	4	0.0	0.0	0.0	−1.1	0.0
3	5	0.0	0.0	0.0	−0.3	−0.1
3	6	0.0	0.0	0.0	−1.0	0.2
4	5	0.0	0.0	0.0	−1.5	0.4
4	6	0.0	0.0	0.0	0.1	0.0
5	6	0.0	0.0	0.0	1.3	−0.4

The elastic coefficients for the tensors used in the following sections are listed in Table 1 in symmetric 6×6 notation (see Babuska & Cara 1991, for the corresponding fourth-order tensor components). Coordinates chosen for the listing are $1 = x$ = E, $2 = y$ = N, $3 = z$ = up, with the fast symmetry axis in the E–W direction or the slow symmetry axis oriented N–S for the two hexagonal cases, and an E–W fast (*a*) and a vertical slow (*b*) axis for all other tensors. The assumed density is 3353 kg m^{-3}.

2.1 Hexagonal case

We start our suite of models with the simple case of hexagonal symmetry (Fig. 1). Hexagonal symmetry refers to a medium with a single fast or slow symmetry axis and isotropic velocities in the plane perpendicular to it. If the axis of symmetry is vertical, this is referred to as transverse isotropy, although the latter term is also used for hexagonal anisotropy with any orientation. Our first test medium has velocities representative of the uppermost mantle and 10 per cent *P* velocity anisotropy (defined here as the difference between the highest and lowest velocity, relative to the average velocity; also called the 'coefficient of anisotropy' *k* after Birch 1960, and equivalent to the definition in Mainprice & Silver 1993). This is in the high range of uppermost mantle values postulated from observations (e.g. Smith & Ekström 1999). The shear wave velocity anisotropy is 9.5 per cent, defined here as the maximum difference between the fast and the slow shear phase velocity relative to the fast shear velocity at the same incidence angle and azimuth. The 4θ term (Backus 1965) is set to zero. Our first test is for hexagonal alignment about the fast axis, with two orientations: first, with the fast symmetry axis aligned horizontally, and secondly, with the symmetry axis dipping by 50°. We calculate all standard observables—*SKS* splitting time and fast direction of splitting, *P* azimuthal traveltime

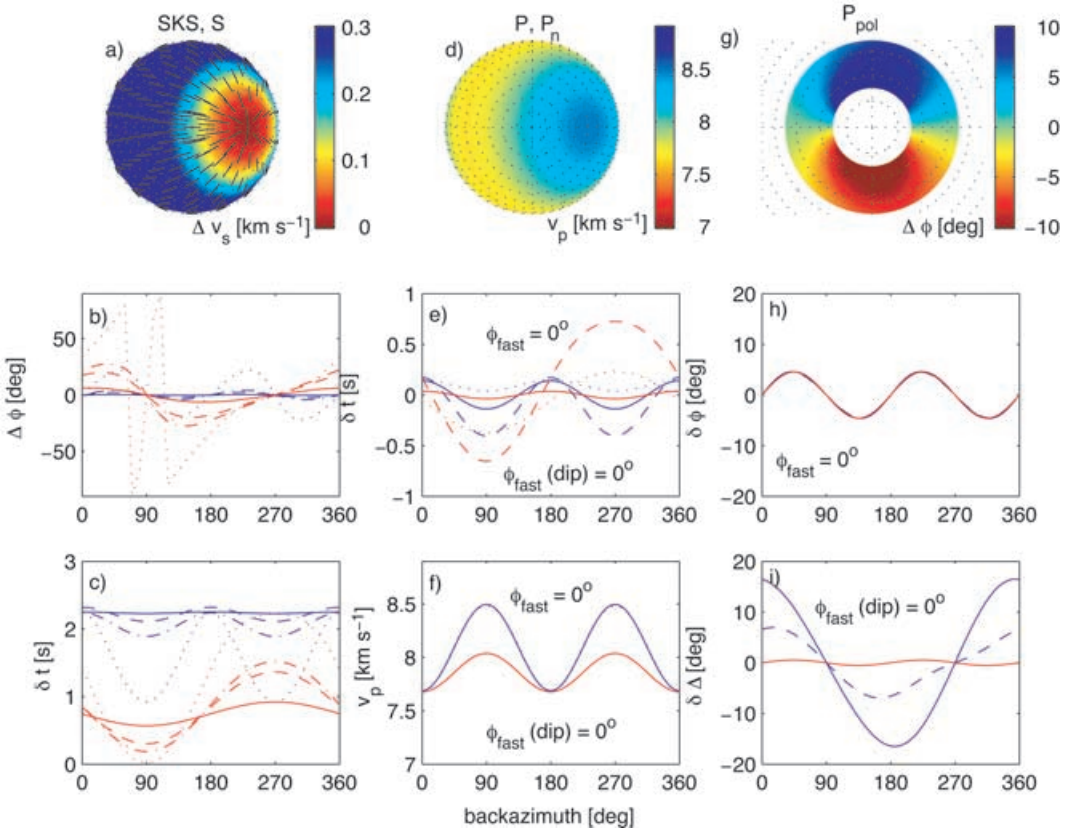

Figure 1. Anisotropy measurements for a hexagonally symmetric medium, E–W fast symmetry axis (left–right in the hemisphere plots). Shear wave splitting is shown in the left-hand column, P and P_n velocity in the middle and $P_{\rm pol}$ on the right. The hemisphere patterns are shown for the dipping case. (a) Fast minus slow shear phase velocity and polarization direction of the fast shear phase on the lower hemisphere. North is up. The azimuth of the fast shear wave polarization is the black line centred on the azimuth/incidence angle. Fast symmetry axis dipping 50° to E. (b) Fast polarization azimuth (clockwise from N), in blue for a horizontal symmetry axis, for *SKS* (solid, shown for 5° incidence angle below the Moho), *SKKS* (dashed, Moho incidence angle $i = 15°$), steep S (dash-dotted, $i = 20°$) and shallow S (dotted, $i = 50°$). In red, the same phases for a symmetry axis dipping 50° to E. (c) The same colour coding for the shear wave splitting delay time for a 100 km thick layer. (d) P velocity pattern on the lower hemisphere for a dipping symmetry axis. (e) P delay times for a 100 km layer for teleseismic ray parameters (dotted, $i = 15°$; dashed, $i = 35°$), in blue for horizontal fast axis orientation and in red for the dipping case. 2θ fits are solid lines in the same colours, $\phi_{\rm fast}$ is the fast axis from the fit. (f) P_n velocity variation (dotted) for the horizontal (blue) and dipping (red) case, and solid 2θ fits in the same colours. (g) $P_{\rm pol}$ anomaly on the lower hemisphere for 15°–35° incidence angle below the Moho for the dipping case. (h) Azimuthal behaviour of $P_{\rm pol}$ for the horizontal case in blue (solid, $i = 15°$; dashed, $i = 35°$ incidence angle) and the 2θ fit in red. (i) Same as (h) for the dipping case.

variation and P_n azimuthal traveltime variation—plus P particle motion deviation.

We calculate splitting times for *SKS* and *SKKS* (from the fast and slow S phase velocities, c_{qS_1} and c_{qS_2}) and the azimuth of the fast split wave (from the fast S particle motion, $\mathbf{a}_{qS_1}$) as a function of the incidence angle and backazimuth. For comparison, we also calculate splitting for S at teleseismic incidence angles.

We show the fast direction for *SKS* and S (Fig. 1b) as well as the splitting delay accumulated travelling through a layer of 100 km thickness (Fig. 1c), taking into account the longer travel paths at shallower incidence angles, in order to facilitate comparison with P delay times and with published splitting delays (the times scale with layer thickness). Each incidence angle and backazimuth yields an individual fast direction and splitting time. The splitting is independent of the incident polarization except for the case when the incident slowness is parallel to the slow or fast S direction. In this case, the orthogonal direction will not be excited, which results in a 'null' splitting observation.

For teleseismic P, we similarly calculate the azimuthal variation in traveltime through a 100 km thick layer from c_{qP} (Fig. 1e). Apart from obtaining a basis for comparison with *SKS* and published P delays based on the maximum absolute delay values, the P traveltime variation with azimuth also allows us to solve for a single fast direction of anisotropy, which can be compared with possibly non-unique (i.e. backazimuth- and incidence angle-dependent) fast directions determined from shear wave splitting. For an E–W horizontal axis of symmetry for instance, the pattern has negative traveltime residuals in E–W and positive residuals in N–S directions, the azimuthal variation is purely cos (2θ), and the fast axis is the location of the minima. We also solve for the same 2θ component in the case of a medium with a dipping fast axis through an azimuthal Fourier decomposition of the delays to test whether the fast azimuth is still resolved correctly.

The same Fourier decomposition procedure is applied to traveltime residuals at near-horizontal incidence, i.e. P_n (Fig. 1f). In this case, we give the percentage azimuthal velocity variation (as above, the difference between the fastest and the slowest relative to the average) to simplify the comparison with published values, and solve for the fast azimuth through harmonic analysis as in the case of P.

The last observable is $P_{\rm pol}$, determined from $\mathbf{a}_{qP}$. In an isotropic medium, the P particle motion is aligned with the backazimuth.

The amount of transverse *P* motion is a measure of the anisotropy of the medium (Schulte-Pelkum *et al.* 2001), and its amplitude and sign vary with backazimuth. For a horizontal axis of symmetry, the maximum azimuthal deviation occurs near 45° off the fast and slow axes, and the fast axis can be determined from the phase of the 2θ component through harmonic analysis as in the case of P_n and *P* times. The azimuthal deviation of $P_{\rm pol}$ is a local effect within the range of one wavelength, rather than being cumulative over the distance travelled through the anisotropic region as in the case of *SKS*, P_n and *P* times. We show the angle of deviation in degrees for the suite of ray parameters swept out by teleseismic *P* (Figs 1h and i).

In the hexagonal case, the fast shear wave direction is parallel to the fast symmetry axis for a horizontal symmetry axis, and is independent of incidence angle and azimuth for the *SKS–SKKS* ray parameter window to within measurement accuracy (Fig. 1b, blue lines). In contrast, *S* shows a distinct azimuthal variation even in the horizontal symmetry case, with fast directions deviating by up to 25° from the fast symmetry axis at shallowest incidence (Fig. 1b, blue dots). The azimuthal variation for both is predominantly 2θ-periodic. The same holds for the splitting time (Fig. 1c); again, the azimuthal variation increases with incidence angle in the horizontal case and is therefore much larger for *S* than for *SKS* and *SKKS*. The average *SKS* splitting delay of about 2 s is comparable to the largest observed values in the literature, consistent with the 10 per cent *P* velocity variation of this model being the upper observed limit for P_n.

In the case of a dipping symmetry axis, a large 1θ-periodic component is added to the azimuthal variation for *SKS*, *SKKS*, *S*, *P* traveltimes and $P_{\rm pol}$, with P_n velocities as the only exception, remaining purely 2θ-periodic as in the horizontally layered case, although with decreased amplitude. The fundamental difference between P_n and the other phases is its azimuthal sampling over a great circle of the slowness sphere, rather than over a minor circle.

While the splitting delay time is decreased compared with the horizontal case, the fast splitting azimuth for a dipping symmetry axis varies by up to 30° for *SKS* and 50° for *SKKS* as a function of backazimuth. It is obvious that in the case of a dipping hexagonal symmetry axis, splitting measurements will not yield the correct fast anisotropy direction unless all backazimuths are considered and the azimuthal variation taken into account. Such a method was introduced by Chevrot (2000). Like our analysis for the *P* phases, it involves Fourier decomposition of the azimuthal behaviour, and would recover the correct fast axis. The harmonic analysis of *P*, P_n and $P_{\rm pol}$ results in the correct fast axis azimuth for the dipping case, although the 2θ-periodic components of *P* and $P_{\rm pol}$ have small amplitudes for high dip angles and may approach the measurement precision for real data.

2.2 Orthorhombic case

Our next test medium consists of 30 per cent aligned olivine and 70 per cent isotropic material. The tensor is constructed by adding $0.3\ c_{ijkl}$ (olivine) $+\ 0.7c_{ijkl}$ (isotropic), where the isotropic part has $v_p = 7.4$ km s^{-1}, $v_s = 4.2$ km s^{-1}, $\rho = 3324$ kg m^{-3}. The olivine monocrystal elastic constants are from Anderson & Isaak (1995) at upper-mantle temperature (700 K) and zero pressure; taking the pressure derivative into account changes the anisotropy by less than 2 per cent at uppermost mantle depths (Mainprice *et al.* 2000). As in the hexagonal case, we start with the fast (*a*) axis aligned horizontally (E–W), and set the slow (*b*) axis vertical ('*b* up') and the intermediate axis (*c*) N–S. We also consider the case of *c* up as well as a dipping fast axis.

All orientations of the orthorhombinc tensor result in observations similar to those for the hexagonal case, the only difference being smaller splitting delays for the horizontal alignment (Fig. 2). The azimuthal behaviour is very close to that for the hexagonal medium, although the 1θ components are stronger for *P* and $P_{\rm pol}$. Again, the harmonic analysis recovers the correct fast axis orientation for both the horizontal and dipping case and for *b* and *c* up, and *SKS* and *SKKS* exhibit significant azimuthal variation for the dipping case, which will bias splitting studies with limited backazimuth range. In contrast to the hexagonal case, the splitting delays show significant 2θ-periodic azimuthal variation even for a horizontal *a* orientation. In the *b* up case, the P_n azimuthal traveltime variation nearly vanishes at 50° dip of the fast axis. Steeper dipping angles lead to a fast axis orientation corresponding to that of the *c* rather than *a* axis. This change reflects the angle at which the horizontal projection of the *a* velocity becomes smaller than the intermediate *c* velocity on the great circle sampled by P_n. For *P* and $P_{\rm pol}$, the same occurs near 80°. The mean fast azimuth for *SKS* remains that of *a* for all dips, but the azimuthal variation becomes very large at the steep dip angles where the *P* phases switch to *c*, so that this geometry is not a viable scenario for a consistent discrepancy between *S* and *P* fast directions. The time delays and $P_{\rm pol}$ values for these models have magnitudes comparable to those typically observed in data.

2.3 Triclinic case

To test whether a more complicated symmetry would result in significantly different observations, we used as our third medium a tensor resulting from crystal grain alignment in a flow model (Blackman *et al.* 2002). 1000 initially randomly oriented grains (70 per cent of which are olivine and 30 per cent orthopyroxene) are put through a strain history to induce a preferential alignment. The models simulate shear induced by upwelling at a mid-ocean ridge followed by horizontal spreading. This can be viewed as horizontal shear strain overprinting alignment from a previous strain regime. We examine the average tensor for a grain assemblage that has travelled away from the ridge for 200 km at a depth of 70 km, to where the texture is no longer influenced by the presence of the ridge. Although the textures at most locations in the flow model are close to orthorhombic (Blackman *et al.* 2002), we chose a triclinic tensor as an end-member. Since the flow model is 2-D, the tensor is predominantly monoclinic with small triclinic components resulting from the initial random grain orientation. We align the tensor with a horizontal E–W fast axis and then a 50° eastward dip as previously. In this case, we take the axis of fastest *P* velocity as the fast axis direction, which corresponds to a horizontal *a* axis in the previous orthorhombic case. There are intermediate and slow axes as in the orthorhombic case, although the axes are no longer mutually orthogonal. As above, we consider orientations that correspond to vertical slow and intermediate axes.

Since the symmetry axes are not orthogonal, aligning the velocity maxima horizontally in the E–W directions leads to an apparent tilt of the intermediate and slow axes from the vertical and from N–S. As a result of their steep angles of incidence, *SKS*, *P* times and $P_{\rm pol}$ reflect the skewness of the axis that is close to vertical, whereas P_n sees that of the approximately horizontal axis. We observe a deviation of the measured fast axis from that of the maximum *P* velocity direction of the order of 20°. However, the fast directions from all teleseismic phases, i.e. from *SKS*, $P_{\rm pol}$ and *P* times, stay

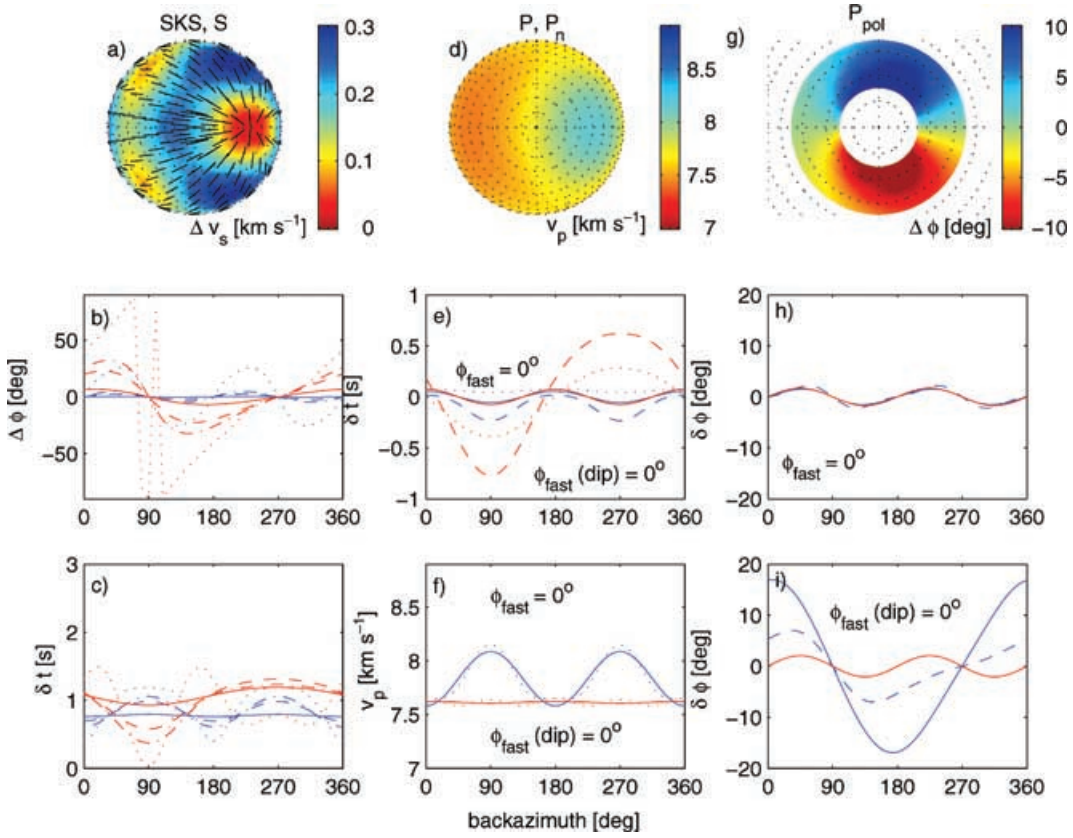

Figure 2. Anisotropy measurements for an orthorhombic medium (30 per cent aligned olivine). Description as in Fig. 1. The results shown are for the case of *c* horizontal N–S and *a* horizontal E–W, and for *a* dipping 50° to the E (hemisphere patterns shown for the latter).

within ∼10° of each other, so that again we see no *P*–*S* discrepancy (Fig. 3).

2.4 Petrological tensors

All tensors considered so far have numerically constructed anisotropy. We calculated the same seismic observables as above for bulk tensors determined for mantle material in laboratory and field analyses to see where in the continuum of simple to complicated symmetries actual mantle samples fall, and how the magnitude of the seismic anisotropy compares with the previous cases.

The first tensors tested were taken from an olivine petrofabric database by Ismaïl & Mainprice (1998). They were determined by measuring grain orientations in olivine aggregates and calculating the Voigt average (the average over rigidities, Babuska & Cara 1991) over all measured grains using the monocrystal elastic constants given by Kumazawa & Anderson (1969) for upper-mantle temperature and pressure. We used the average tensors for samples from subduction zones, fast spreading ridges and kimberlites. The results are similar for all three sample types; as an example, we show the average fast spreading ridge case in Fig. 4. All three averages look very similar to the orthorhombic case, with anomaly magnitudes comparable to or even slightly larger than the 30 per cent aligned olivine tensor. It is not unreasonable to suspect that a more complicated symmetry may occur in some samples but that it is averaged out over the database, therefore we also analysed tensors calculated for xenoliths from three individual locations in the Canadian Cordillera and Alaska by Ji *et al.* (1994). While Ismaïl & Mainprice (1998) only considered olivine, Ji *et al.* (1994) measured the orientation of olivine, orthopyroxene and clinopyroxene grains and formed the Voigt average over all, taking into account the pressure and temperature dependence of the individual elastic constants. The results again show no significant departure from orthorhombic symmetry. The anomaly amplitudes are slightly smaller than for the olivine database tensors, which is to be expected since pyroxenes usually align in such a way that they counter the anisotropy contribution from olivine (Carter 1976).

3 MULTILAYERED MODELS

We now extend the media under consideration from homogeneous to layered cases. Layering introduces a frequency dependence to the results. Rather than systematically testing the behaviour of the observables as a function of frequency, we limit this discussion to the frequency bands relevant for actual data in each observable: *SKS* in the period range from 3 to 20 s (pulse width of 6 s) and P_{pol} at periods larger than 10 s. P_n is not discussed in this section, since it is assumed to sample the topmost layer in the same manner as in the homogeneous case. The modelling for *SKS*, *P* traveltimes and P_{pol} was performed using a code based on the layer matrix method by Kennett (1983) with anisotropic extensions following Chapman & Shearer (1989) and Booth & Crampin (1985). We calculate the harmonic response of a horizontal layer stack to an incident plane wave over a range of frequencies (0–5 Hz) to obtain a pulse seismogram (i.e. a series of delta functions, here at $\Delta t = 0.1$ s) via an inverse Fourier transform. Then we apply bandfilters to construct synthetic seismograms. This method is equivalent to a reflectivity formulation apart from an integration over slowness, which in our

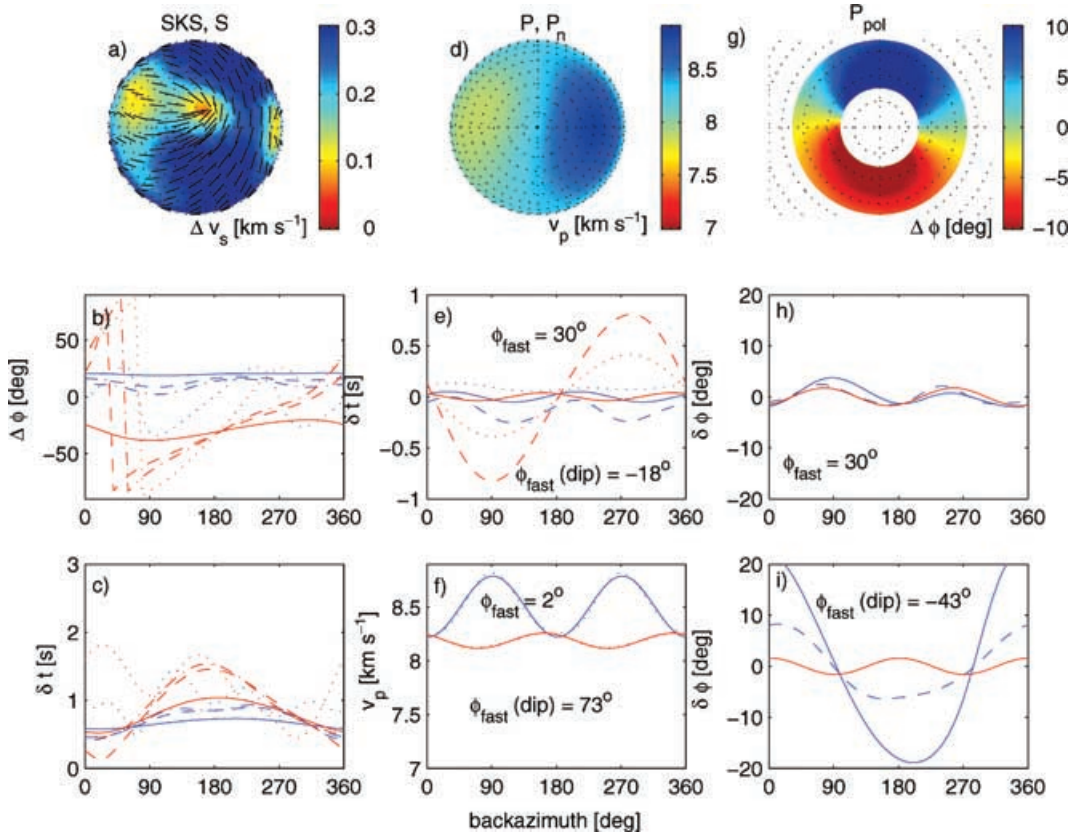

Figure 3. Anisotropy measurements for a triclinic medium. Description as in Fig. 1.

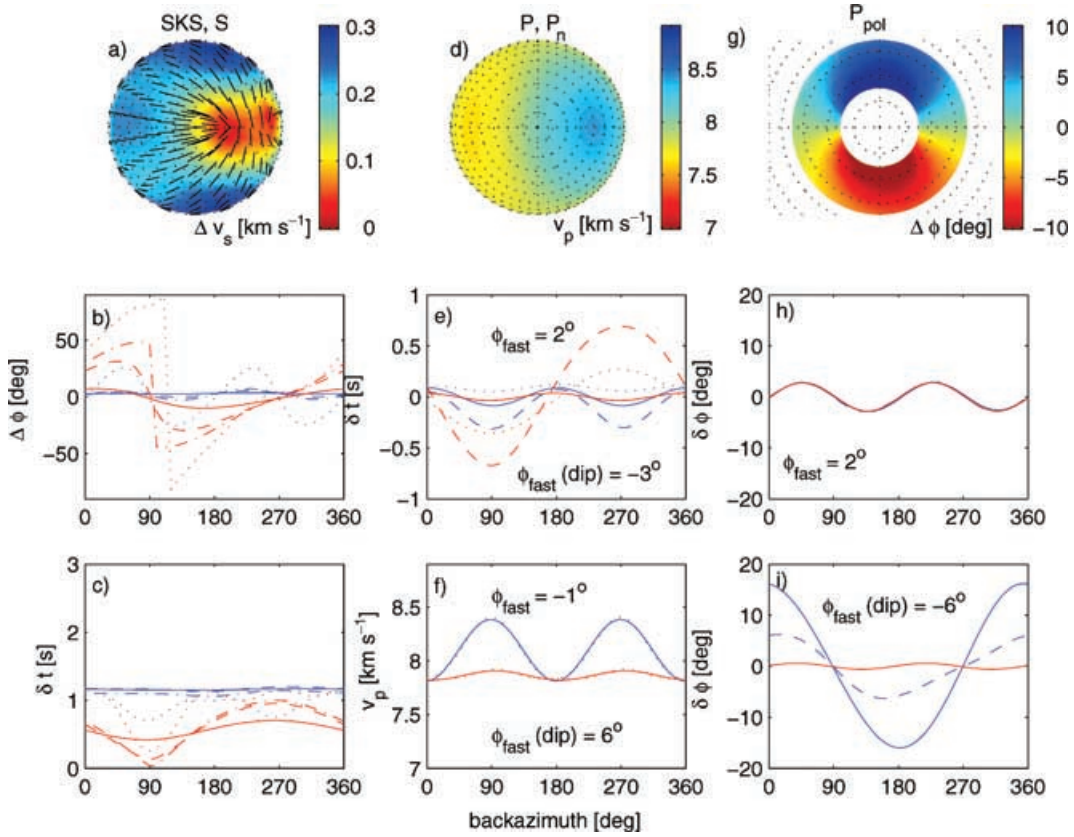

Figure 4. Anisotropy measurements for a petrological tensor. Description as in Fig. 1.

case of plane waves is superfluous. The horizontal layers can have anisotropy of general symmetry and orientation, and we vary the backazimuth and the incidence angle of the incoming plane *P* or *S* waves.

In contrast to the homogeneous case, where the polarizations and phase velocities (and therefore delays) are the direct numerical result of solving the eigenproblem, the analysis in the layered case requires taking measurements off the synthetics in the same way as done for actual data. We analyse our filtered three-component synthetics as follows.

For shear phases, we employ a splitting analysis similar to those used in Bowman & Ando (1987) and Levin *et al.* (1996). The two horizontal components are rotated into a radial and transverse component relative to each value of backazimuth in increments of 1°, and cross-correlated with a range of time-shifts of the transverse component towards the radial one. Rotation of the radial component on to the fast axis and the transverse one on to the slow axis results in two identical pulses separated by the delay time between the fast and slow *S* phase. Thus the backazimuth and time-shift that result in the maximum cross-correlation between the components indicate the fast axis and splitting time. Since we are now performing an actual splitting measurement, rather than calculating the fast and slow shear phase directions of the medium as in the homogeneous case, the polarization of the incoming phase becomes relevant in that splitting will not be measured if the incident polarization is along the fast or slow shear polarization, and the amplitude of the split phases in each layer will depend on the orientation of the incident shear wave relative to the fast and slow direction in that layer. We set the incident polarization to radial for both *SKS–SKKS* and for teleseismic *S*. While the incident polarization direction affects the location of splitting nulls, it is the backazimuth of the incident wave that affects the measured fast direction and splitting time. This is sometimes obscured in the literature when *SKS* is assumed to be radially polarized and therefore 'polarization' is used synonymously with 'backazimuth'.

To measure *P* polarization azimuths, we take a 40 s window around the *P* arrival (corresponding to the first cycle of the motion) on all three components. We form the covariance matrix between the components and solve its eigenproblem. The eigenvector associated with the largest eigenvalue gives the particle motion or polarization direction of the onset. This time-domain analysis was introduced by Jurkevics (1988).

Teleseismic *P* traveltimes were determined from the location of the first delta pulse in the vertical component of the unfiltered synthetic. As a test, we verified these times against arrival times measured using a cross-correlation technique on filtered arrivals as employed in long-period traveltime studies (Bolton & Masters 2001) for a range of layered models with anisotropy. We determined that there is no noticeable distortion of the pulse on the vertical component due to anisotropy. The largest effect is from crustal reverberations at the tail end of the onset, and the arrival time is still recovered correctly. This implies an absence of frequency dependence of the *P* arrival time on anisotropy, since filtering out the high frequencies has no effect on the picks.

The measurements for all phases were also verified against the numerical eigenproblem solution in the homogeneous or single-layer case. For $P_{\rm pol}$ and *P* traveltimes, the rest of the analysis is performed as in the homogeneous layer case, i.e. via a harmonic decomposition of the residuals over azimuth to determine the fast azimuth from the 2θ phase.

3.1 Two hexagonal layers with horizontal fast axes

We begin our exploration of the layer stack case with a model with two anisotropic layers of 60 km thickness each (Fig. 5). This model may be regarded as a thin lithosphere and asthenosphere, or two lithospheric layers. Both layers have hexagonal symmetry with a horizontal fast symmetry axis, where the fast axis azimuth of one layer is rotated in the horizontal plane relative to that of the other.

SKS shows a 4θ variation of the apparent fast azimuth and splitting time with backazimuth that is characteristic for splitting in multiple layers (e.g. Silver & Savage 1994; Rümpker & Silver 1998), and is an effect of the initial polarization (set to radial here); in the hexagonal case, there is little dependence on the incidence angle.

For $P_{\rm pol}$, the localized nature of the polarization change in *P* cumulative becomes apparent, in contrast to the cumulative behaviour of shear wave splitting. The recovered fast azimuth is that of the top layer, and is independent of the orientation of the bottom layer, provided the top layer thickness is at least of the order of a wavelength at the frequency considered. For the horizontal hexagonal case, the azimuthal variation of the horizontal particle motion is purely 2θ. Phase and amplitude are identical to that generated by the top layer by itself, and independent of its thickness provided it is of the order of one wavelength or more. The results are also independent of the incidence angle in this case. In contrast to *P* times and *SKS*, the anisotropic effects on $P_{\rm pol}$ also vanish when the wave front continues into an isotropic region, since at the anisotropic–isotropic boundary the non-longitudinal motion of *qP* converts to *SH*. The addition of a thin isotropic layer at the top dampens the anomaly amplitude for $P_{\rm pol}$, and an isotropic layer thick enough to separate the *P–SH* converted phase from direct *P* by more than a cycle will remove the $P_{\rm pol}$ anomaly of the initial *P* motion entirely.

Teleseismic *P* traveltimes, on the other hand, exhibit cumulative behaviour similar to *SKS*. The residual pattern is purely 2θ for layers with horizontal hexagonal symmetry, but the phase and amplitude are determined by the interference between the 2θ patterns of the individual layers, which depends on the relative orientation of the fast directions and the layer thicknesses. For two layers with the same strength of hexagonal anisotropy but different fast axis azimuths, the apparent fast azimuth is the exact average of the two layer orientations weighted by the thicknesses. Also, the residuals are dependent on the ray parameter, since a shallower incidence results in more traveltime difference being accumulated in each anisotropic layer.

3.2 Depth sensitivity

Saltzer *et al.* (2000) documented that for vertical incidence, *SKS* apparent fast directions are biased towards the upper portion of the model in typically measured frequency bands. Our results indicate the same for the entire *SKS* and *SKKS* incidence angle range. For two layers of equal thickness, each exceeding one wavelength corresponding to the pulse width ($\sim$30 km), the 4θ pattern is centred on the fast azimuth of the upper layer. When the upper layer thickness approaches a wavelength, the average fast azimuth changes to that of a thicker bottom layer. This behaviour is also influenced by the amount of splitting incurred in the bottom layer.

P traveltimes average linearly over the layers and are therefore weighted more towards the fast azimuth of the bottom layer than *SKS*. In contrast, $P_{\rm pol}$ is more sensitive to the top layer than *SKS*

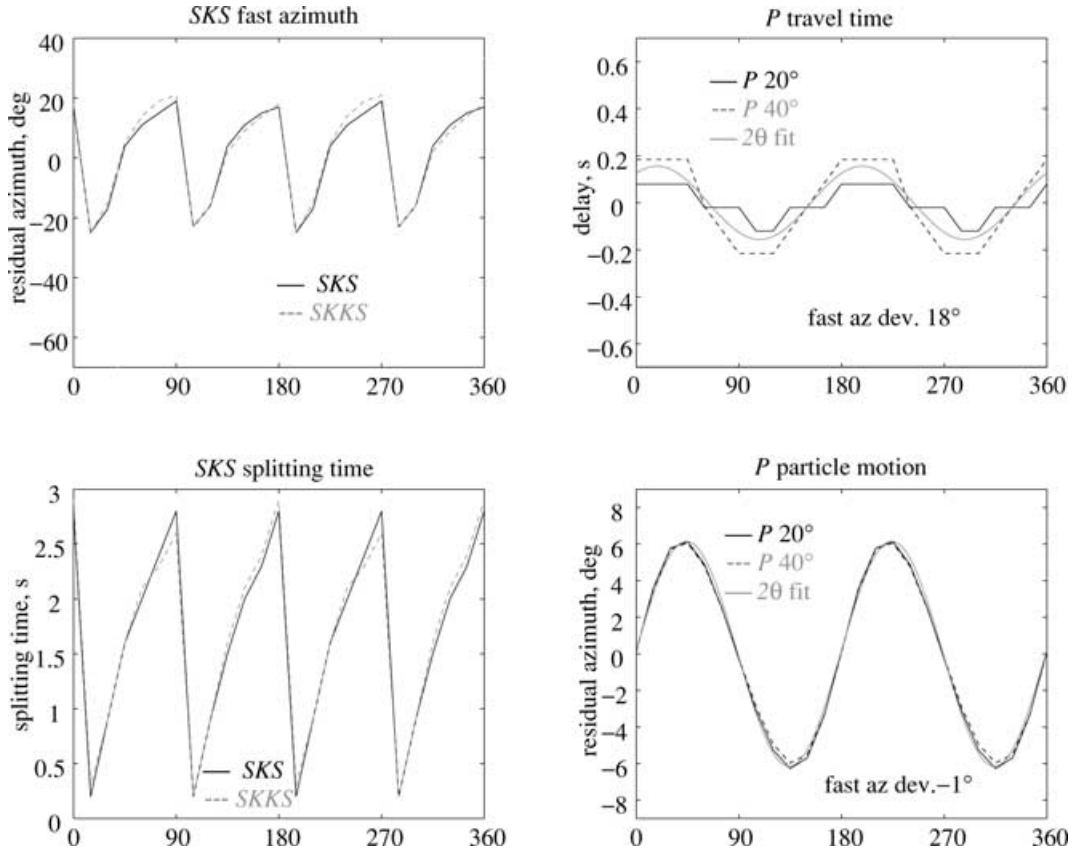

Figure 5. Results for two hexagonal layers with 10 per cent hexagonal anisotropy and horizontal fast symmetry axes. Both layers have 60 km thickness, the fast azimuth is E–W in the upper layer and rotated to 40° S of E in the lower layer. Top left: shear wave fast azimuths at incidence angles of 5° (solid black) and 15° (dashed grey). The residuals are relative to the E–W true fast azimuth. Bottom left: shear wave splitting delay times, legend same as for fast azimuths. Top right: *P* delay times for uppermost mantle incidence angles (solid black, 20°; dashed grey, 40°; the 0.1 s time step in the synthetics is visible) and a 2θ fit (solid grey). The residual fast azimuth indicated is relative to the true E–W fast direction. (bottom right) $P_{\rm pol}$ anomaly, legend same as for *P* delay times.

and the fast azimuth will be accurately recovered even for a top layer thickness of ∼30 km when *SKS* already senses the bottom layer. When ranking depth sensitivity from shallower to deeper, the order would therefore be P_n, $P_{\rm pol}$, *SKS*, *P* times, as illustrated in Fig. 6.

3.3 Hexagonal dipping and multiple layers

The observations made above for all phases also hold for three or more layers with hexagonal horizontal symmetry. In the two-layer hexagonal case, a dip of the symmetry axis of one or both layers adds a 1θ component to *P* traveltimes and to *SKS* splitting delays and apparent fast directions. The 1θ contribution to $P_{\rm pol}$ remains minuscule and so does the dependence on the ray parameter, and the 2θ component of $P_{\rm pol}$ still yields the fast azimuth of the top layer. For *P*, the 1 and 2θ components are in phase, and the averaging behaviour of the fast azimuth is no longer linear with respect to layer thickness. The relative phase between the 1 and 2θ components may be a candidate for a discriminant between 1θ signals generated by dipping anisotropy or by isotropic heterogeneity. However, we show below that for lower symmetry classes of dipping anisotropy, the 1 and 2θ components do not remain in phase.

The variation of *SKS* fast directions with ray parameter remains close to the measurement accuracy (3°–5°, Levin *et al.* 1999) for most azimuth ranges, but the splitting times show a distinct dependence. In particular, the apparent null directions occur at different backazimuths. Near these backazimuths, the apparent fast direction also varies significantly with ray parameter.

3.4 Orthorhombic symmetry

SKS results for two orthorhombic layers (here 30 per cent aligned olivine) with horizontal fast axes show an additional 2θ dependence, compared with only 4θ in the hexagonal case. The results also become ray-parameter-dependent in that the 2θ dependence is more pronounced for shallower incidence angles. As in the hexagonal case, the fast azimuth 4θ pattern is centred about the fast axis azimuth of the upper layer. $P_{\rm pol}$ and *P* traveltimes in the orthorhombic horizontal fast axis case behave much like in the equivalent hexagonal case: $P_{\rm pol}$ recovers the top layer fast azimuth and is independent of the ray parameter, while *P* delays show the mean fast azimuth and are larger for shallower incidence angles. When a fast axis dip is added, the *P* times show a strong 1θ component as in the hexagonal case. However, the 1 and 2θ components are now out of phase. For $P_{\rm pol}$, the 1θ contribution remains small, though it is larger than in the hexagonal case and may be measurable, and there is still little ray parameter dependence. The phase of the 2θ component for both $P_{\rm pol}$ and *P* times is not affected so that the measured fast axis azimuths are the same as those determined for the non-dipping case.

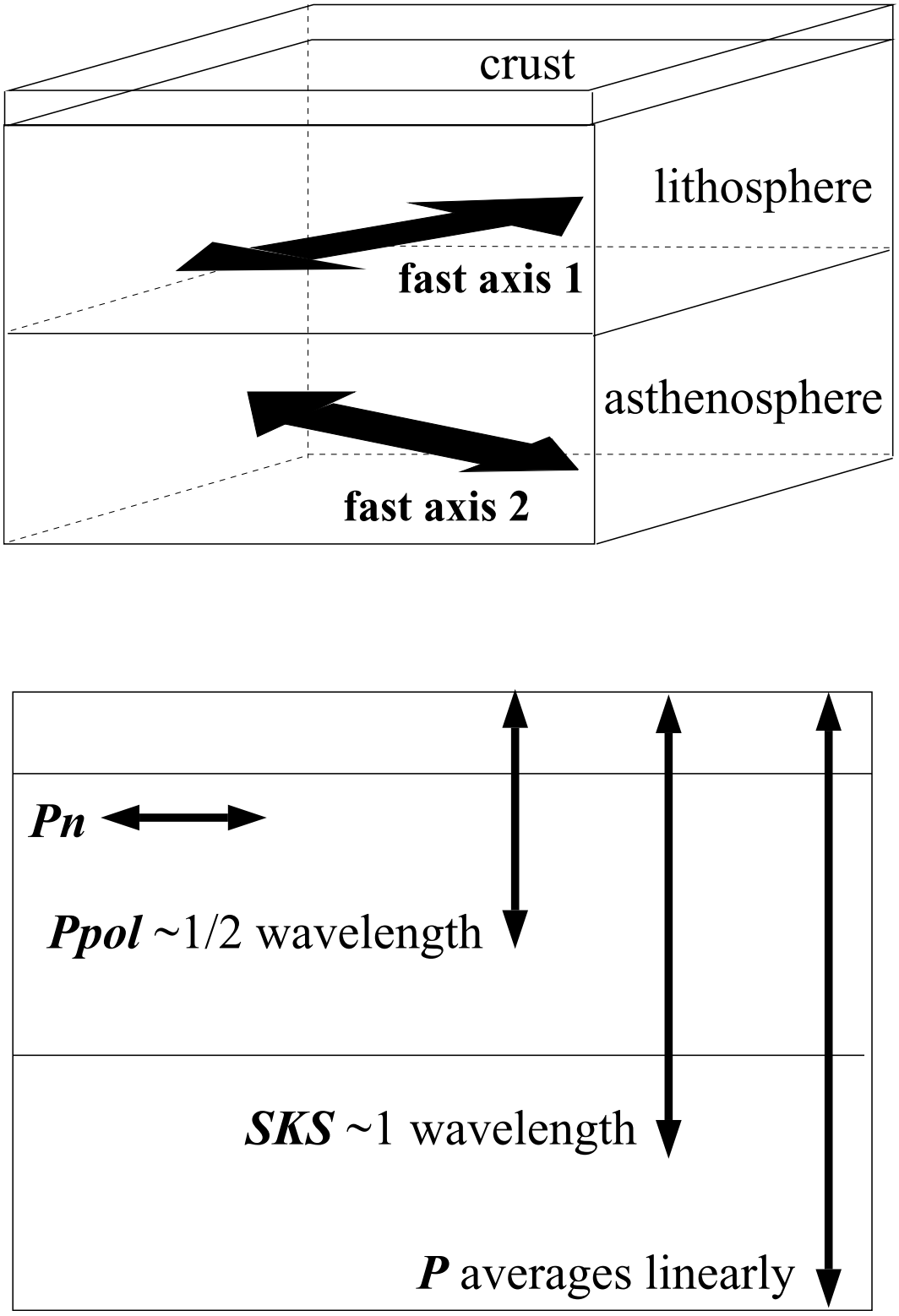

Figure 6. Illustration of the differences in depth sensitivity for seismic phases used to diagnose mantle anisotropy. Top: we calculated synthetic seismograms for a model consisting of two anisotropic layers with different fast axis orientations beneath an isotropic crust. Bottom: our results indicate that P_n at short epicentral distances samples the mantle immediately underneath the Moho, *P* polarization is sensitive to anisotropy within half wavelength of the surface, *SKS* fast polarization is dominated by the top wavelength and *P* traveltimes average linearly over the raypath.

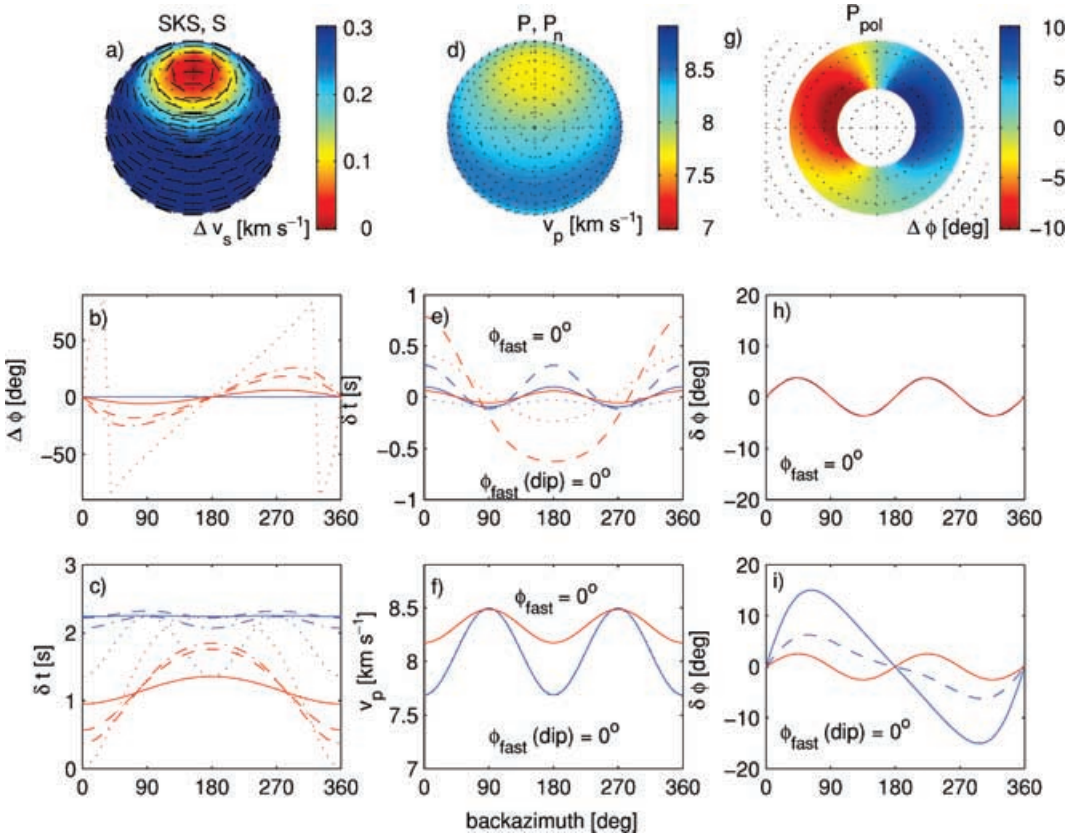

Figure 7. Results for two triclinic layers, the upper with 7 per cent anisotropy and 40 km thickness, the lower with 11 per cent anisotropy and 80 km thickness. The fast azimuth is E–W in the top layer and rotated to 30° S of E in the bottom layer. Legend same as for Fig. 5.

SKS in the dipping case also shows an additional 1θ component, mostly in the splitting times, but the average fast azimuth remains that of the upper layer.

3.5 Triclinic symmetry

As in the homogeneous case above, we consider layers of the triclinic flow model tensor as the most complicated end-member of anisotropic symmetries. The tensor orientation is defined by the direction of the fastest axis, which in the triclinic case has no other symmetry axes orthogonal to it. We show the results of a two-layer model where the upper and lower layer have anisotropy described by two different tensors calculated in the flow model described in Section 2.3. The top layer has 7 per cent *P* velocity anisotropy and the bottom layer has 11 per cent anisotropy. The upper layer has a thickness of 40 km and an E–W fast axis, the lower layer has a horizontal fast axis rotated 30°N of E and is 80 km thick. *SKS* splitting delays now show a strong 1 and 2θ dependence, while the fast directions remain mostly 4θ. The 1 and 2θ azimuthal behaviour of the fast splitting direction becomes more visible for an additional fast axis dip (Fig. 7). P_{pol} and *P* times now also exhibit a 1θ component and ray parameter dependence in the horizontal symmetry case, although the ray parameter dependence for P_{pol} is close to the resolution limit (∼1°). To within ∼5°, the 2θ fast azimuth is again that of the top layer for P_{pol} and the layer average for *P* times. This remains the same when a dip of the fast axis is added, despite a 1θ dependence that becomes significant for P_{pol} and predominant for *P* times.

4 THE *P–S* PARADOX OR LACK THEREOF

None of the models studied above exhibit near-orthogonal apparent fast directions of *S* versus *P* anisotropy. A certain school in the literature (e.g. Plomerova *et al.* 1996; also Babuska *et al.* 1993; Guilbert *et al.* 1996; Plomerova *et al.* 1998, 2001; Babuska & Plomerova 2001; hereinafter, we cite Plomerova *et al.* 1996 as representative of this school) reports such observations, and uses a specific model of anisotropy to explain these cases. The model has hexagonal symmetry with a slow symmetry axis rather than a fast one as considered above. Such a symmetry may develop for an olivine assemblage under uniaxial compression (Christensen & Crosson 1968), where the slow *b*-axis takes on a preferential direction, while the fast and intermediate *a*- and *c*-axes are randomly oriented in a plane perpendicular to *b*. Mantle rock samples, however, appear to show fast axis alignment (Christensen 1984), which develops under simple shear, and slow axis hexagonal alignment has not been reported.

The homogeneous eigenproblem solutions for slow axis alignment are shown in Fig. 8. This is the dipping slow axis case that is given in Plomerova *et al.* (1996) and others as an explanation for near-orthogonal *P* and *SKS* fast azimuths. However, we show that it is really the definition of the fast *P* direction that leads to a contradiction. Plomerova *et al.* (1996) see 1θ ('bipolar') patterns of *P* traveltimes and call the azimuth of the traveltime minimum the fast *P* direction, although this is actually the azimuth of the slow *b* axis, and the fast azimuth for *P* is that of the *a–c* plane orthogonal to it (see Fig. 9). In the scenario of Plomerova *et al.* (1996), *SKS*

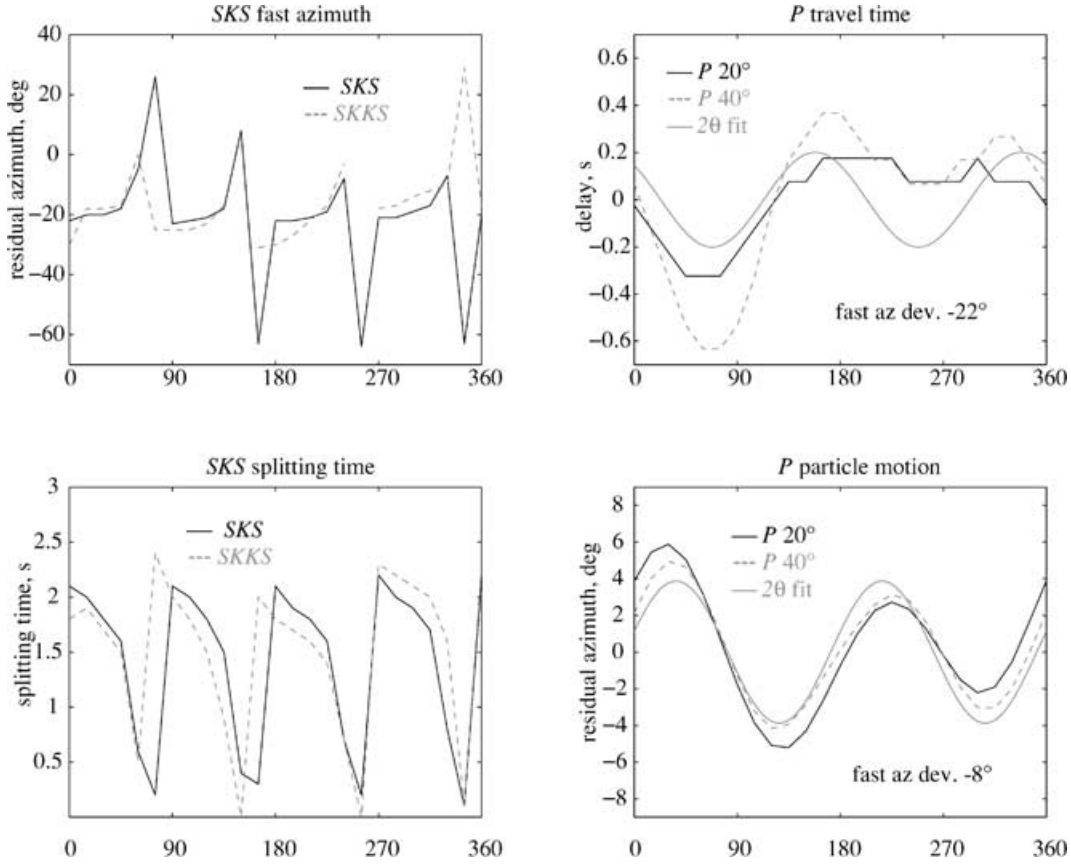

Figure 8. Anisotropy measurements for a hexagonal medium with a slow dipping symmetry axis. The *P* velocity anisotropy is 10 per cent, the slow axis dips 50° to N. Legend as in Fig. 1.

sees the *a*–*c* azimuth and *P* the *b* azimuth, therefore they arrive at a 90° discrepancy. However, if instead of calling the minimum of the 1θ component in *P* the 'fast' axis as in Plomerova *et al.* (1996), the fast direction is determined as described above from the phase of the 2θ component, *P* times also recover the *a*–*c* plane orientation as the fast azimuth. With this analysis method, we see no apparent contradiction between *SKS* and *P* fast directions. The fast direction common to *SKS* and *P* times also agrees with that determined from $P_{\rm pol}$ and P_n.

One may regard the apparent discrepancy observed by Guilbert *et al.* (1996), Makeyeva *et al.* (1990), Plomerova *et al.* (1996), etc. as a semantics issue concerning the definition of 'fast *P*', if it were not for at least one set of studies where this explanation may be insufficient. If the *P* traveltime fast direction is determined from the 2θ phase, rather than from that of 1θ, and turns out to be parallel to P_n and $P_{\rm pol}$ fast azimuths but orthogonal to *SKS* fast azimuths, then we have a true discrepancy which cannot be explained by a slow hexagonal symmetry with dip nor with layering. This situation may exist in central Europe, for instance. The *SKS* fast azimuth has been determined in multiple studies to be close to E–W (see the compilations in Brechner *et al.* 1998; Granet *et al.* 1998). P_n, on the other hand, has been consistently shown to have fast directions closer to N–S (Enderle *et al.* 1996; Bamford 1977; Smith & Ekström 1999). The fast direction inferred from $P_{\rm pol}$ agrees with the N–S alignment from P_n (Schulte-Pelkum *et al.* 2001). Plomerova *et al.* (1998) found velocity maxima for teleseismic *P* in northerly and southerly directions in 'bipolar' (i.e. 1θ) residual patterns. Wylegalla *et al.* (1988) performed an azimuthal Fourier analysis of *P* residuals and arrived at a N–S orientation of anisotropy based on the 2θ component. If the analysis in Wylegalla *et al.* (1988) is correct, then this would be a true case of contradictory fast *P* and *S* directions. However, the study does not include corrections for source and path effects not related to anisotropy, and its 1θ directions do not coincide with those seen by Plomerova *et al.* (1998). At the present stage, it seems prudent to refrain from declaring the conclusive existence of a *P* and *S* fast direction discrepancy.

5 CONCLUSIONS

In many areas, current data availability would allow a more thorough study of anisotropy than traditional *SKS* splitting, by considering azimuthal variation and incidence angle dependence of splitting and by adding *P*-wave observables to the analysis. *SKS* splitting results are dependent on backazimuth and angle of incidence in all but the horizontally symmetric hexagonal case. If dip is introduced, or if the symmetry is orthorhombic or even lower, azimuthal dependence has to be taken into account. In general, the dependence is stronger for shallower incidence angles so that caution should be used when adding teleseismic *S* to *SKS* results. Bulk tensors derived from both laboratory tests and from strain texturing have largely orthorhombic symmetry, and show predicted anisotropy amplitudes comparable to published observations. Even when picking lower symmetry end-members of the flow model tensors and using dipping symmetry axes, the fast directions derived from different body wave measurements are mutually consistent. We were unable to find a model that produces a discrepancy of nearly 90° between mean *SKS* fast

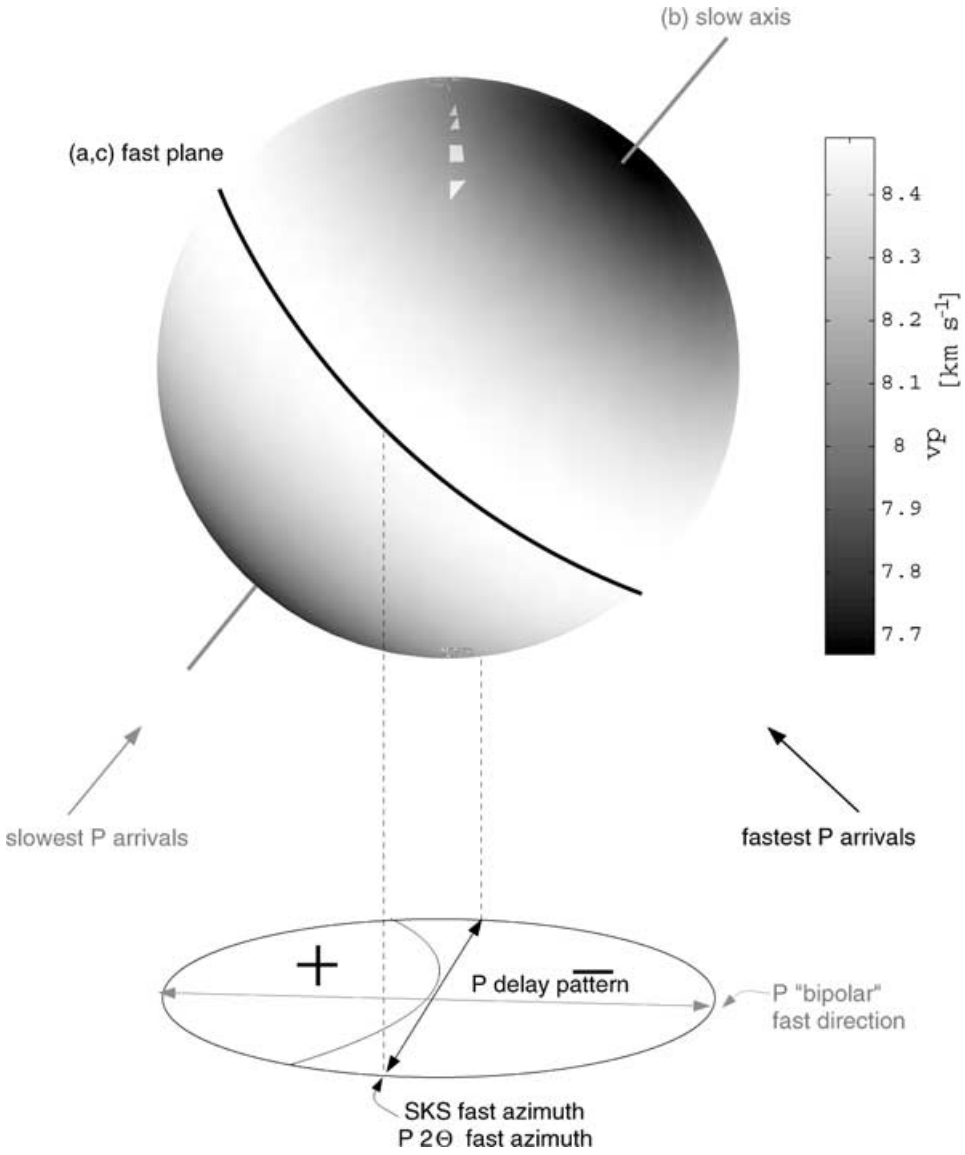

Figure 9. Illustration of the apparent *P* versus *S* fast direction paradox. The sphere shows the *P* velocity pattern for a hexagonally symmetric model with a dipping slow axis. The fast shear azimuth, fast 2θ *P* azimuth, and 'bipolar' *P* traveltime residual pattern ('+' for late, '−' for early arrivals) and fast 1θ *P* direction are indicated on the horizontal projection below the sphere.

directions and fast *P* azimuths. This was despite testing a range of models including complicated symmetries and layered models. The cases presented as such discrepancies in the literature reduce to the definition of what constitutes a fast *P* azimuth, rather than a consistent difference in the anisotropy seen by *P* compared with shear waves. We propose that so far, there is no conclusive evidence that the latter exists. There is a difference in depth sensitivity for the phases under consideration, but rather than separating into *P* and *S* phases, the bias toward shallower anisotropy becomes progressively larger in the order of teleseismic *P* traveltimes, *SKS* splitting, $P_{\rm pol}$ and P_n.

ACKNOWLEDGMENTS

We thank Peter Shearer, Guy Masters and Michael Kendall for insightful discussions, and Peter Shearer for providing anisotropic reflectivity routines. Suggestions by Karen Fischer, Eric Sandvol and Steven Ward significantly improved the manuscript. This work was supported by NSF grant EAR-9902422.

REFERENCES

Anderson, O. & Isaak, D.G., 1995. Elastic constants of mantle minerals at high temperature, in, *A Handbook of Physical Constants: Mineral Physics and Crystallography,* Vol. 2, pp. 64–98, ed. Ahrens, T., AGU Handbook, AGU, Washington, DC.

Babuska, V. & Cara, M., 1991. *Seismic Anisotropy in the Earth,* Kluwer, Dordrecht.

Babuska, V. & Plomerova, 2001. Subcrustal lithosphere around the Saxothuringian–Moldanubian suture zone—a model derived from anisotropy of seismic wave velocities, *Tectonophysics,* **332,** 185–199.

Babuska, V., Plomerova, J. & Sileny, J., 1984. Spatial variations of *P* residuals and deep structure of the European lithosphere, *Geophys. J. R. astr. Soc.,* **79,** 363–383.

Babuska, V., Plomerova, J. & Sileny, J., 1993. Models of seismic anisotropy in the deep continental lithosphere, *Phys. Earth planet. Inter.,* **78,** 167–191.

Backus, G.E., 1965. Possible forms of seismic anisotropy of the uppermost mantle under oceans, *J. geophys. Res.,* **70,** 3429–3439.

Bamford, D., 1977. P_n velocity anisotropy in a continental upper mantle, *Geophys. J. R. astr. Soc.,* **49,** 29–48.

Birch, F., 1960. The velocity of compressional waves in rocks to 10 kilobars, *J. geophys. Res.,* **65,** 1083–1102.

Blackman, D.K., Wenk, H.R. & Kendall, J.M., 2002. Seismic anisotropy of the upper mantle: 1. Factors that affect mineral texture and effective elastic properties, *G-Cubed,* **3,** U1–U24.

Bolton, H. & Masters, G., 2001. Travel times of *P* and *S* from the global digital seismic networks: implications for the relative variation of *P* and *S* velocity in the mantle, *J. geophys. Res.,* **106,** 13 527–13 540.

Booth, D.C. & Crampin, S., 1985. The anisotropic reflectivity technique: theory, *Geophys. J. R. astr. Soc.,* **72,** 31–45.

Bowman, J.R. & Ando, M.A., 1987. Shear-wave splitting in the upper mantle wedge above the Tonga subduction zone, *Geophys. J. R. astr. Soc.,* **88,** 24–41.

Brechner, S., Klinge, K., Krüger, F. & Plenefisch, T., 1998. Backazimuthal variations of splitting parameters of teleseismic *SKS* phases at broadband stations in Germany, *Pure appl. Geophys.,* **151,** 305–331.

Carter, N.L., 1976. Steady state flow of rocks, *Rev. Geophys. Space Phys.,* **14,** 301–360.

Chapman, C.H. & Shearer, P.M., 1989. Ray tracing in azimuthally anisotropic media—II. Quasi-shear wave coupling, *Geophys. J.,* **96,** 65–83.

Chevrot, S., 2000. Multichannel analysis of shear wave splitting, *J. geophys. Res.,* **105,** 21 579–21 590.

Christensen, N.I., 1984. The magnitude, symmetry and origin of upper mantle anisotropy based on fabric analysis of ultramafic tectonites, *Geophys. J. R. astr. Soc.,* **76,** 89–111.

Christensen, N.I. & Crosson, R.S., 1968. Seismic anisotropy in the upper mantle, *Tectonophysics,* **6,** 93–107.

Dziewonski, A.M. & Anderson, D.L., 1983. Travel times and station corrections for *P* waves at teleseismic distances, *J. geophys. Res.,* **88,** 3295–3314.

Enderle, U., Mechie, J., Sobolev, S. & Fuchs, K., 1996. Seismic anisotropy within the uppermost mantle of southern Germany, *Geophys. J. Int.,* **125,** 747–767.

Frederiksen, A. & Bostock, M., 2000. Modelling teleseismic waves in dipping anisotropic structures, *Geophys. J. Int.,* **141,** 401–412.

Granet, M., Glahn, A. & Achauer, U., 1998. Anisotropic measurements in the Rhinegraben area and the French Massif Central: geodynamic implications, *Pure appl. Geophys.,* **151,** 333–364.

Gresillaud, A. & Cara, M., 1996. Anisotropy and *P*-wave tomography: a new approach for inverting teleseismic data from a dense array of stations, *Geophys. J. Int.,* **126,** 77–91.

Guilbert, J., Poupinet, G. & Mei, J., 1996. A study of azimuthal *P* residuals and shear-wave splitting across the Kunlun range (Northern Tibetan plateau), *Phys. Earth planet. Inter.,* **95,** 167–174.

Hearn, T.M., 1996. Anisotropic P_n tomography in the western United States, *J. geophys. Res.,* **101,** 8403–8414.

Hearn, T.M., 1999. Uppermost mantle velocities and anisotropy beneath Europe, *J. geophys. Res.,* **104,** 15 123–15 139.

Ismaïl, W.B. & Mainprice, D., 1998. An olivine fabric database: an overview of upper mantle fabrics and seismic anisotropy, *Tectonophysics,* **296,** 145–157.

Ji, S., Zhao, X. & Francis, D., 1994. Calibration of shear-wave splitting in the subcontinental upper mantle beneath active orogenic belts using ultramafic xenoliths from the Canadian Cordillera and Alaska, *Tectonophysics,* **239,** 1–27.

Jurkevics, A., 1988. Polarization analysis of three-component array data, *Bull. seism. Soc. Am.,* **78,** 1725–1743.

Kendall, J.-M., 2000. Seismic anisotropy in the boundary layers of the Earth's mantle, in *Earth's Deep Interior: Mineral Physics and Tomography From the Atomic to the Global Scale, Geophysical Monograph Series,* Vol. 117, 149–175, eds Karato, S. *et al.*, AGU, Washington, DC.

Kennett, B.L.N., 1983. *Seismic Wave Propagation in Stratified Media,* Cambridge University Press, New York.

Kumazawa, M. & Anderson, O.L., 1969. Elastic moduli, pressure derivatives, and temperature derivatives of single-crystal olivine and single-crystal forsterite, *J. geophys. Res.,* **74,** 5961–5972.

Levin, V. & Park, J., 1997. *P–SH* conversions in a flat-layered medium with anisotropy of arbitrary orientation, *Geophys. J. Int.,* **131,** 253–266.

Levin, V., Menke, W. & Lerner-Lam, A., 1996. Seismic anisotropy in the north-eastern US as a source of significant teleseismic *P* travel time anomalies, *Geophys. J. Int.,* **126,** 593–603.

Levin, V., Menke, W. & Park, J., 1999. Shear wave splitting in the Appalachians and the Urals: a case for multilayered anisotropy, *J. geophys. Res.,* **104,** 17 975–17 993.

Mainprice, D. & Silver, P.G., 1993. Interpretation of *SKS*-waves using samples from the subcontinental lithosphere, *Phys. Earth planet. Inter.,* **78,** 257–280.

Mainprice, D., Barruol, G. & Ismail, W.B., 2000. The seismic anisotropy of the Earth's mantle, in *Earth's Deep Interior: Mineral Physics and Tomography From the Atomic to the Global Scale, Geophysical Monograph Series,* Vol. 117, pp. 237–264, eds Karato, S. *et al.*, AGU, Washington, DC.

Makeyeva, L.I., Plesinger, A. & Horalek, J., 1990. Azimuthal anisotropy beneath the Bohemian Massif from broad-band seismograms of *SKS* waves, *Phys. Earth planet. Inter.,* **62,** 298–306.

Montagner, J.-P., Pommera, D.-A. & Lavé, J., 2000. How to relate body wave and surface wave anisotropy?, *J. geophys. Res.,* **105,** 19 015–19 027.

Plomerova, J., Sileny, J. & Babuska, V., 1996. Joint interpretation of upper-mantle anisotropy based on teleseismic *P* travel time delays and inversion of shear-wave splitting parameters, *Phys. Earth planet. Inter.,* **95,** 293–309.

Plomerova, J., Babuska, V., Sileny, J. & Horalek, J., 1998. Seismic anisotropy and velocity variation in the mantle beneath the Saxothuringicum–Moldanubicum contact in Central Europe, *Pure appl. Geophys.,* **151,** 365–394.

Plomerova, J., Arvidsson, R., Babuska, V., Granet, M., Kulhanek, O., Poupinet, G. & Sileny, J., 2001. An array study of lithospheric structure across the Protogine zone, Värmland, south-central Sweden—signs of a paleocontinental collision, *Tectonophysics,* **332,** 1–21.

Rümpker, G. & Silver, P.G., 1998. Apparent shear-wave splitting parameters in the presence of vertically varying anisotropy, *Geophys. J. Int.,* **135,** 790–800.

Saltzer, R.L., Gaherty, J.B. & Jordan, T.H., 2000. How are vertical shear wave splitting measurements affected by variations in the orientation of azimuthal anisotropy with depth?, *Geophys. J. Int.,* **141,** 374–390.

Savage, M.K., 1999. Seismic anisotropy and mantle deformation: what have we learned from shear wave splitting?, *Rev. Geophys.,* **37,** 65–106.

Savage, M.K. & Silver, P.G., 1993. Mantle deformation and tectonics: constraints from seismic anisotropy in the western United States, *Phys. Earth planet. Inter.,* **78,** 207–227.

Schulte-Pelkum, V., Masters, G. & Shearer, P.M., 2001. Upper mantle anisotropy from long-period *P* polarization, *J. geophys. Res.,* **106,** 21 917–21 934.

Shearer, P.M., 1999. *Introduction to Seismology,* Cambridge University Press, New York.

Silver, P.G., 1996. Seismic anisotropy beneath the continents: probing the depths of geology, *Annu. Rev. Earth planet. Sci.,* **24,** 385–432.

Silver, P.G. & Savage, M.K., 1994. The interpretation of shear-wave splitting parameters in the presence of two anisotropic layers, *Geophys. J. Int.,* **119,** 949–963.

Smith, G.P. & Ekström, G., 1999. A global study of P_n anisotropy beneath continents, *J. geophys. Res.,* **104,** 963–980.

Wylegalla, K., Bormann, P. & Baumbach, M., 1988. Investigation of inhomogeneities and anisotropy in the crust and upper mantle of central Europe by means of teleseismic *P* waves, *Phys. Earth planet. Inter.,* **51,** 169–178.